

CONVERTING CT-SCAN IMAGES INTO RESISTIVITY MEASUREMENTS TO FORM AN ANATOMICAL ATLAS FOR ELECTRICAL IMPEDANCE TOMOGRAPHY

Erick Darío León Bueno de Camargo, edlbcamargo@yahoo.com.br

Fernando Silva de Moura, fernandosmoura@gmail.com

Olavo Luppi Silva, olavo.luppi@usp.br

Flavius Portella Ribas Martins, flavius.martins@poli.usp.br

Raúl Gonzalez Lima, lima.raul@gmail.com

Department of Mechanical Engineering - Polytechnic School of University of São Paulo, São Paulo, Brazil

Marcelo Britto Passos Amato, amato@unisys.com.br

Faculty of Medicine of University of São Paulo, São Paulo, Brazil

Ana Carolina Brandão de Campos Fonseca Pinto, anacarolina@usp.br

Surgery Department - Faculty of Veterinary Medicine of University of São Paulo, São Paulo, Brazil

Abstract. *Electrical Impedance Tomography is a non invasive medical imaging technique used to infer living tissue impeditivity from surface electrical measurements. Mathematically this is an ill-posed non-linear inverse problem. An anatomical atlas based on the impeditivity of the tissue can be used as a regularization method for solving the inverse problem. Computed Tomography images (CT-Scan) and in vivo measurements of tissue impeditivity of swine thorax performed by our group and from published data were used. The CT-scan images must be segmented so that the electrical properties of each tissue can be used to obtain images. This work utilizes the real part of the impeditivity, the resistivity, only. The process of mapping, segmenting and converting CT-Scan images into gray scale resistivity images is documented. These resistivity distribution images are then used to estimate the statistics of the probabilistic model of clinically probable images, also called anatomical atlas.*

Keywords: *anatomical atlas, electrical impedance tomography, tissue resistivity*

1. INTRODUCTION

Electrical Impedance Tomography (EIT) is used to estimate the impeditivity distribution within a domain. The estimation process uses a set of electrical potential measurements acquired from its boundary through a certain number of electrodes when low-power high-frequency electrical currents is imposed through through the same set of electrodes. EIT has many applications like hemorrhage detection, breast cancer detection, visualization of multiphase flow, crack detection on mechanical components and trees monitoring, for instance Holder (2005); Kerner *et al.* (2002); Kim *et al.* (2007). In general, EIT focus on estimating the impeditivity distribution, that is, a complex valued function within a domain. In cases which the imaginary component can be omitted, EIT is used to estimate the resistivity distribution. This work investigates EIT for resistivity distributions.

Kaipio and Somersalo (2004) presents the theoretical background to solve a EIT inverse problem using Baye's theorem of conditional probabilities. In this framework, the inverse problem is conceived as the problem of finding the conditional probability distribution of the resistivity distribution, given the measurements and some prior information concerning the problem. It can be written as Eq. (1),

$$\pi(\rho | v, c) \propto \pi(\rho)\pi(v|\rho, c) \quad (1)$$

where $\pi(\rho | v, c)$ is the conditional probability density function of occurrence of the resistivity distribution ρ , given the electrical potential distribution v and the current injection distribution c , $\pi(\rho)$ is the prior probability density function of occurrence of the resistivity distribution in certain population and $\pi(v | \rho, c)$ is the conditional probability density function of occurrence of the electric potential distribution v given the resistivity distribution and the current injection distribution. The last is also called the likelihood function. The prior probability density function $\pi(\rho)$ can be interpreted as a probabilistic description of the solution space of the inverse problem and may be estimated from sampled data.

Most of the swine chest tissue impeditivity data present in the literature was measured *in vitro* (Gabriel *et al.*, 1996). Therefore they do not reflect the variations of these properties caused by ventilation or blood perfusion. These variations must be measured *in vivo*, with appropriate electronics and probes. The probes must avoid large hemorrhages where they are inserted otherwise the excess of blood would affect the tissue impeditivity measurement. Previous works on probe configurations suggest the use of four electrodes, two of these used for current injection and the other two for electrical

potential measurements, avoiding the measurement errors caused by the contact impedance between the tissue and the electrode, see Tsai *et al.* (2000); Steendijk *et al.* (1993); Paulson *et al.* (2004); Kinouchi *et al.* (1997).

Several priors can be used in EIT. The non-negativeness prior is used when the resistivity is known to be not negative (de Lima *et al.*, 2007). Smoothness priors are used when the resistivity distribution is known to have smooth spatial distribution, for these cases, Gaussian low pass filters are frequently used (Adler and Guardo, 1996). The (minimal) total variation prior is used when the resistivity distribution is known to have a few, yet abrupt spatial variations (Borsic *et al.*, 2010).

Beside these priors, anatomy based priors have the characteristic of being smooth where the variations are expected to be smooth and sharp where the variations are expected to be sharp. They carry on the information about the statistics of the resistivity distribution within a certain population. Therefore, the use of anatomy based priors should improve the spatial resolution and the resistivity resolution since they convey different the smoothness information for different regions of the domain of interest Ω . Additionally, an anatomy based prior can be estimated using a sampling methodology and does not require the search for a regularization parameter.

The mathematical feasibility of anatomy-based priors was shown for Sobolev spaces $H^1(\Omega)$ (the space of piecewise linear functions), since in space $H^0(\Omega)$ (the space of piecewise constant functions) the computation of directional derivatives of the electrical property are cumbersome (Kaipio *et al.*, 1998).

The present work describes the development of anatomy and physiology based prior for lung monitoring of swine chests. Continuous monitoring of the human chest, as an assistance for protective lung ventilation protocol, is the long term objective of the present work. The experience gathered developing the prior for swine chests may be used for developing a human chest prior in the future, without using *in vivo* measurements. The benefits of such prior is shown through a numerical example.

1.1 Objectives and methodology

The main objective of the present work is to estimate a prior probability density function of swine chest tissues resistivity distribution for EIT. Additionally, the CT-Scan image segmentation process is described and *in vivo* tissue resistivity information, presented in a companion paper, is added in order to compute such probability density function.

The methodology is divided in two major tasks, segmentation of anatomical structures from a data bank of swine chest CT-Scan images and the estimation of the anatomy based prior statistics.

1.2 Bank of CT-scans images from pig thorax

Thirty nine swine chest CT-Scan data sets from 25 different animals from Pneumology Laboratory of Faculty of Medicine of University of São Paulo were used in this study. There are more sets than animals because some of them were scanned in two or more lung conditions. The 8th thoracic vertebrae were used to align all data sets. Examples of CT-Scan images can be viewed in Fig. 1. By a CT-Scan set we mean a set of images of the same animal thorax, at different transversal planes within 100 mm, centered at 8th thoracic vertebrae. Each CT-Scan image represent a slice with thickness of 1.0 mm or 1.6 mm, depending on the CT-Scan equipment.

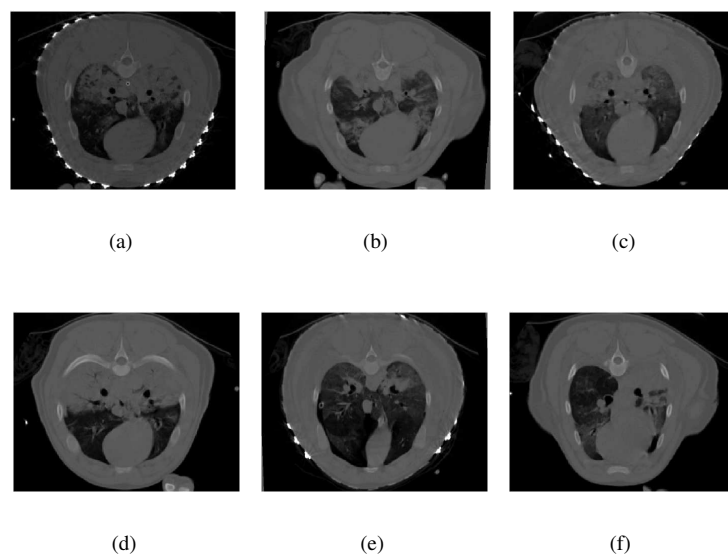


Figure 1. CT-scan samples from swine thoraxes at the 8th thoracic vertebrae for six different animals

Due to the relatively small number of animals, an artificial number of swine CT-Scan was generated following these steps:

1. All images of each set were classified in five groups, in correspondence to its position. Group A if the image plane is situated within the interval $[-50, -30[$ (in millimeters, relative to the 8th thoracic vertebrae), group B within $[-30, -10[$, group C within $[-10, 10[$, group D within $[10, 30[$ and group E within $[30, 50]$. Figure 2 shows the elements of Group C for a given swine;

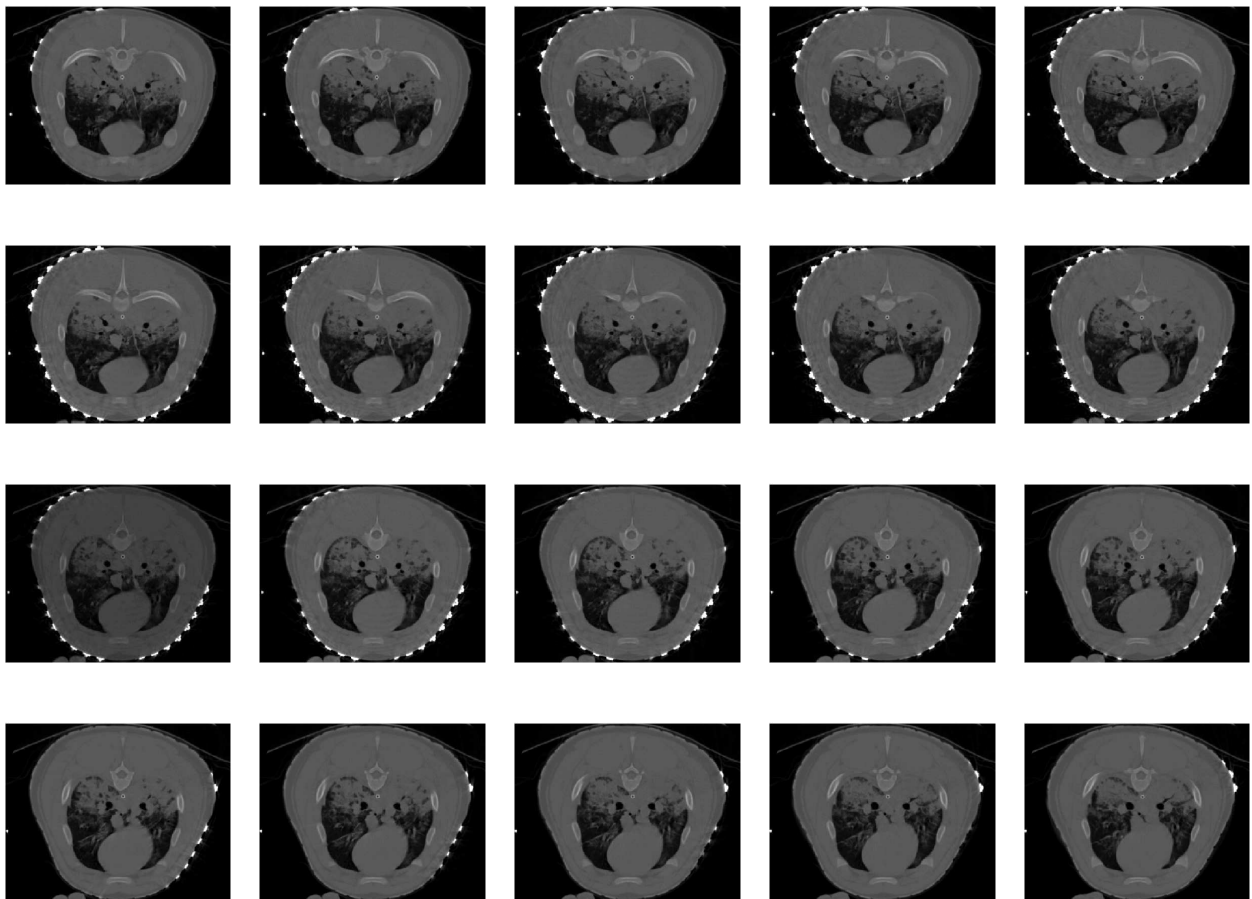
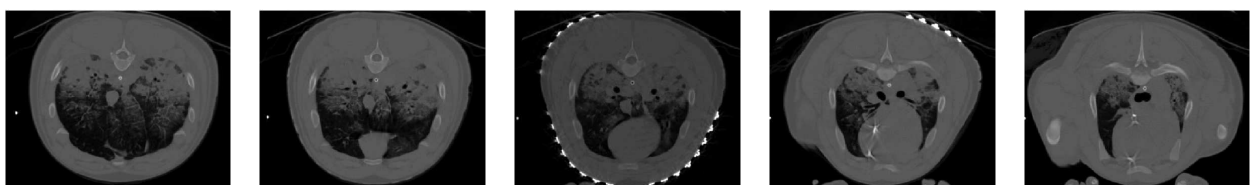


Figure 2. CT-scan slices of Group A

2. One element of each group is selected. It is considered that such five-element subset represents a CT-Scan of a different *virtual* swine. Each image of this set represents now a 20-millimetre slice of the thorax on transversal plane. A subset can be seen in (Fig. 3);



(a) Element from group A.

(b) Element from group B.

(c) Element from group C.

(d) Element from group D.

(e) Element from group E.

Figure 3. CT-Scan set of a virtual swine (256x327x5 pixels).

3. This process is repeated for all 39 CT-scans.

Proceeding this way, a total of 660 3-dimensional images were segmented. Although this procedure introduces a artificial correlation between images, these are different enough and this approximation can be used. This procedure helps to increase the covariance matrix rank.

1.3 Determination of a common domain

In order to register 660 images from different subjects, in different conditions and at different heights related to 8th vertebrae, it is necessary to map all images to a common domain. The advantages of this procedure are

1. Eliminate the external undesired artifacts observed around the thorax image, i.e., the surgical blankets (bright arcs at the bottom of the image), animal's inferior limbs (one or two small blobs over the thorax) and the artificial circular envelope caused by the CT image windowing algorithm;
2. Measure the images obtained in the previous step according to a proper metric in order to scale them to a common size;
3. Identify the parameters of an affine transformation to properly scale, translate and rotate all the images generated;
4. Construct the average contour based on the contours of all images generated in step 3.

Once pixel values in CT-scan images are tissue dependent, undesirable artifacts can be removed with a thresholding algorithm at chosen levels. This is followed by a chain of morphological operators (Serra, 1989) properly designed to separate the region delimited by the regularized chest contour from the remaining artifacts. Figure 4 illustrates three steps of this morphological-based artifacts removal algorithm. After thresholding the original image Fig. 1(a) into gray level Fig. 4(a), the black regions inside the white zones are removed with a "fill-holes" algorithm Haralick and Shapiro (1991). As a result, a group of genus-0 objects emerge Fig. 4(b). Finally, an opening operation using a circle of radius 45 pixels as the structuring element removes all the smaller and thinner objects around the main one, without promoting any significant change in its shape Fig. 4(c).

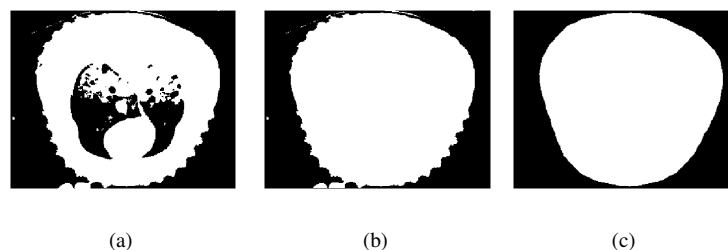


Figure 4. (a) Application of thresholding. (b) Application of 'fill-holes' algorithm. (c) Application of opening operation.

The next step is to scale all images to the same dimension based on some anatomical landmark. Two anatomical landmarks were considered, (i) the bounding box of skin contour and (ii) the bounding box defined by right and left ribs, sternum bone and the spinous process of 8th vertebra. The later was chosen due to the greater variability associated of skin contours. Figure 5 shows the process of scaling Fig. 1(a).

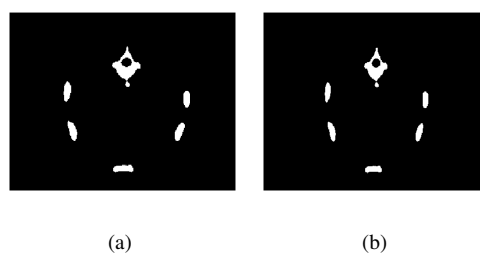


Figure 5. Scaling based on the mean size of the rib cage. (a) Before scaling. (b) After scaling.

The average contour is generated by selecting pixels present in more than 50% of segmented images. This can be determined by computing the mean contour image of all subjects and selection only those with more than 50% of the maximum value of this mean image. The mean image and the average contour can be seen in Fig. 6.

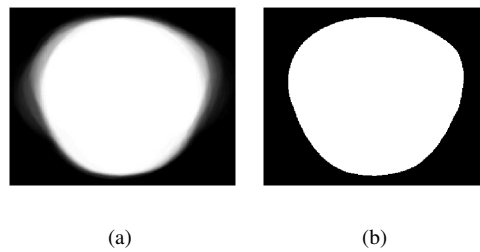


Figure 6. (a) Mean contour image; (b) Average contour.

1.4 Tissue image segmentation

Three different tissues – bones, lungs and other tissues – were identified according to their brightness characteristics (Fig. 7). It is classified as 'other tissues' everything else that is not bone or lung. The segmentation is done with a manual thresholding followed by a chain of morphological operators, to eliminate undesirable artifacts and regularize boundaries.

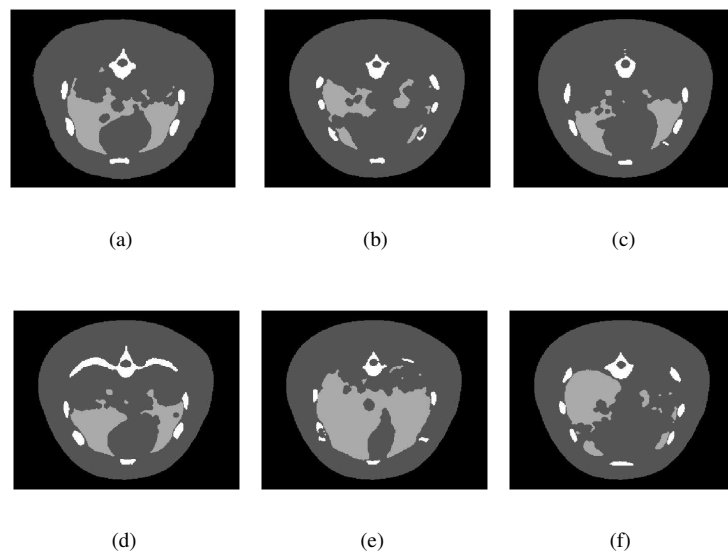


Figure 7. Figures 1a to 1f after segmentation: bones (white), other tissues (dark gray) and lungs (light gray)

1.5 Impedivity measurements

For the present work, three tissues were considered, namely, lungs, bones and other tissues. Here we consider 'other tissues' resistivity the same of muscles resistivity. Bone experimental resistivity value was obtained from literature (Gabriel *et al.*, 1996), while experimental resistivity values for muscles and lungs were measured at Surgery Department - Faculty of Veterinary Medicine of University of São Paulo which is presented in a companion paper for COBEM 2011. The values are presented on Tab. 1. The standard deviation of the bone was unknown and was set to 1.0.

Table 1. Tissue resistivities in Ωm

Tissue	mean value	std. dev.
Muscles	2.59	0.51
Lungs	8.14	1.55
Bone	30.0	1.0

1.6 Approximating anatomical atlas statistics

The segmented tomographic images represents a sample of the spatial distribution of three different tissues with three different gray levels, while the impedance measurements associates each tissue with an impeditivity value, which in turn is related with the gray levels of segmented image. This data can be used to approximate the anatomy based prior statistics for EIT.

For each subject, identified by an index $j = 1, \dots, N_p$, let its segmented 3-dimensional CT-Scan X_j be partitioned in $t = 1, 2, \dots, N_t$ (not necessarily connected) regions $\Omega_{t,j}$. For each region $\Omega_{t,j}$, let $\mathcal{X}_{t,j}$ be its characteristic function, defined as

$$\mathcal{X}_{t,j} = \begin{cases} 1 & \text{if } x \in \Omega_{t,j} \\ 0 & \text{otherwise} \end{cases}, \quad (2)$$

where x is the coordinate vector of a pixel within the image. Define a matrix $[\mathcal{X}_j]$ with $\mathcal{X}_{t,j}$ as its columns.

Let the statistics of the electrical resistivity ρ_t of all N_t tissues be known and given by their probability density functions (pdf) π_t , for $t = 1, 2, \dots, N_t$. It is assumed that all ρ_t are Gaussian and independent of each other. Let a random vector $\boldsymbol{\rho} \in \mathbb{R}^{N_t}$ be composed by all resistivities and let $\bar{\boldsymbol{\rho}}$ and $\boldsymbol{\Gamma}_{\boldsymbol{\rho}_t}$ be its expectancy and covariance matrix.

Given a sample $\boldsymbol{\rho}_s$, drawn from these pdfs, a sample image X_j^s can be formed by using the characteristic functions, multiplied by the sampled resistivities

$$X_j^s = \sum_{t=1}^{N_t} \rho_{t,s} \mathcal{X}_{t,j} = [\mathcal{X}_j] \boldsymbol{\rho}_s. \quad (3)$$

For a large number of subjects N_p and a large number of samples N_s , the statistics of the anatomical atlas for the whole population can be approximated by computing the sample statistics of all samples X_j^s for all N_p subjects. This process can be simplified analytically, without the need of explicitly generating the samples for each subject.

One approximation often assumed is that the anatomical atlas is a Gaussian random variable, so it is completely described by its expectancy $\bar{\mathbb{X}}$ and covariance $\boldsymbol{\Gamma}_{\mathbb{X}}$. The expectancy is estimated by

$$\begin{aligned} \bar{\mathbb{X}} &= \frac{1}{N_p N_s} \left(\sum_{s=1}^{N_s} X_1^s + \sum_{s=1}^{N_s} X_2^s + \dots + \sum_{s=1}^{N_s} X_{N_p}^s \right) = \\ &= \frac{1}{N_p} \sum_{j=1}^{N_p} \left(\frac{1}{N_s} \sum_{s=1}^{N_s} X_j^s \right) = \frac{1}{N_p} \sum_{j=1}^{N_p} \bar{X}_j, \end{aligned} \quad (4)$$

where \bar{X}_j is the sample mean image of the j -th subject

$$\bar{X}_j = E\{X_j^s\} = [\mathcal{X}_j] \bar{\boldsymbol{\rho}}_t. \quad (5)$$

The covariance $\boldsymbol{\Gamma}_{\mathbb{X}}$ is estimated by

$$\begin{aligned} \boldsymbol{\Gamma}_{\mathbb{X}} &= \frac{1}{N_p N_s - 1} \sum_{j=1}^{N_p} \left(\sum_{s=1}^{N_s} (X_j^s - \bar{\mathbb{X}})(X_j^s - \bar{\mathbb{X}})^T \right) = \\ &= \frac{N_s - 1}{N_p N_s - 1} \sum_{j=1}^{N_p} \boldsymbol{\Gamma}_j + \frac{N_s}{N_p N_s - 1} \sum_{j=1}^{N_p} (\bar{X}_j - \bar{\mathbb{X}})(\bar{X}_j - \bar{\mathbb{X}})^T, \end{aligned} \quad (6)$$

where $\boldsymbol{\Gamma}_j$ is the sample covariance matrix of the j -th subject

$$\boldsymbol{\Gamma}_j = E\{(X_j^s - \bar{X}_j)(X_j^s - \bar{X}_j)^T\} = E\{[\mathcal{X}_j](\boldsymbol{\rho}_s - \bar{\boldsymbol{\rho}}_t)(\boldsymbol{\rho}_s - \bar{\boldsymbol{\rho}}_t)^T[\mathcal{X}_j]^T\} = [\mathcal{X}_j] \boldsymbol{\Gamma}_{\boldsymbol{\rho}_t} [\mathcal{X}_j]^T. \quad (7)$$

At the limit $N_s \rightarrow \infty$, both fraction in Eq. (6) before sums tend to $\frac{1}{N_p}$. Defining $\Delta X_j = \bar{X}_j - \bar{\mathbb{X}}$, Eq. (6) can be written as

$$\boldsymbol{\Gamma}_{\mathbb{X}} = \frac{1}{N_p} \sum_{j=1}^{N_p} ([\mathcal{X}_j] \boldsymbol{\Gamma}_{\boldsymbol{\rho}_t} [\mathcal{X}_j]^T + \Delta X_j \Delta X_j^T) = \frac{1}{N_p} \sum_{j=1}^{N_p} \mathbf{W}_j \mathbf{Y} \mathbf{W}_j^T \quad (8)$$

$$\mathbf{W}_j = \begin{bmatrix} [\mathcal{X}_j] & \Delta X_j \end{bmatrix} \quad (9)$$

$$\mathbf{Y} = \begin{bmatrix} \boldsymbol{\Gamma}_{\boldsymbol{\rho}_t} & \mathbf{0} \\ \mathbf{0} & 1 \end{bmatrix}. \quad (10)$$

Finally, this equation can be written in factorized form as

$$\Gamma_{\mathbb{X}} = \frac{1}{N_p} \sum_{j=1}^{N_p} (\mathbf{W}_j \sqrt{\mathbf{Y}}) (\sqrt{\mathbf{Y}} \mathbf{W}_j)^T = \mathbf{K} \mathbf{K}^T \quad (11)$$

$$\mathbf{K} = \frac{1}{\sqrt{N_p}} [\mathbf{W}_1 \sqrt{\mathbf{Y}} \quad \mathbf{W}_2 \sqrt{\mathbf{Y}} \quad \dots \quad \mathbf{W}_{N_p} \sqrt{\mathbf{Y}}]. \quad (12)$$

where $\sqrt{\mathbf{Y}}$ is a square root matrix of \mathbf{Y} .

1.7 The use of the anatomy based prior for image estimation

The algorithm for the image estimation is based on a Gauss–Newton iterative search method (Vauhkonen, 2004). Our algorithm minimizes a performance index Eq. (13) which is composed by three terms

$$I = (\mathbf{v}_m - \mathbf{v}_p(\boldsymbol{\rho}))^T (\mathbf{v}_m - \mathbf{v}_p(\boldsymbol{\rho})) + \alpha (\boldsymbol{\rho} - \bar{\boldsymbol{\rho}})^T \mathbf{F}^T \mathbf{F} (\boldsymbol{\rho} - \bar{\boldsymbol{\rho}}) + \gamma (\boldsymbol{\rho} - \bar{\boldsymbol{\rho}})^T (\boldsymbol{\Gamma} + \sigma^2 \mathbf{I})^{-1} (\boldsymbol{\rho} - \bar{\boldsymbol{\rho}}) \quad (13)$$

where \mathbf{v}_m is a set of measured electrical potentials at the electrodes, \mathbf{v}_p is a set of predicted electrical potentials at the electrodes computed by the Finite Elements Method (FEM), $\boldsymbol{\rho}$ is a vector containing the resistivity of all finite elements, α is the regularization parameter of a Gaussian high-pass filter \mathbf{F} , $\boldsymbol{\Gamma}$ is the covariance matrix of the anatomy based prior, interpolated to the FEM mesh, $\bar{\boldsymbol{\rho}}$ is the expected vector of the anatomy based prior also interpolated to the FEM mesh, γ is a regularization parameter for the anatomy based prior and σ is the variance of a uncorrelated Gaussian white noise added to the covariance matrix.

The first term takes into account the measurements, a candidate resistivity distribution $\boldsymbol{\rho}$ and the Finite Elements model of the domain. It penalizes the difference between measurements and the prediction of the numerical model. The second term is the Euclidean norm of the high-pass filtered difference between a candidate image $\boldsymbol{\rho}$ and the statistically expected image $\bar{\boldsymbol{\rho}}$. It penalizes spatial high frequency image components of this difference vector. The third term is the anatomy based prior which minimizes the difference between a candidate image $\boldsymbol{\rho}$ and the statistically expected image $\bar{\boldsymbol{\rho}}$ pondered with the inverse of the covariance matrix.

2. Results

Anatomy based prior

Figure 8 shows the mean image computed from the segmented CT-scan of all $N_p = 660$ subjects.

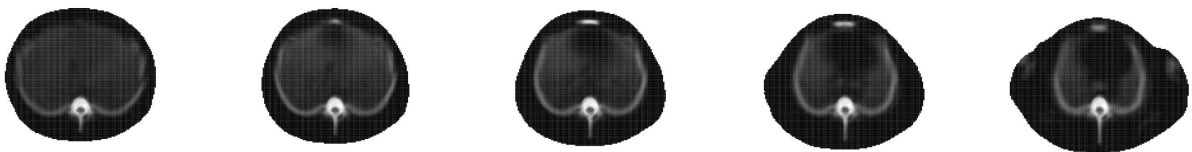


Figure 8. Mean image $\bar{\mathbb{X}}$ obtained from the anatomical atlas.

Expected resistivity distribution

Figure 9 shows the simulated resistivity distribution. The FEM mesh contains 1.2 million elements. The resistivity distribution was generated from a CT-Scan of an animal which was not included in the set used to compute the anatomical atlas. This distribution considers only resistivities of the same three tissues segmented for the atlas.



Figure 9. Simulated image used to simulate electrical potential measurements.

Obtained resistivity images

Figure 10 to Fig. 13 show the results of Gauss-Newton algorithm with different values of regularization parameters for a mesh with 9500 elements. All initial guesses were the same uniform resistivity distribution of $5.0 \Omega\text{m}$.

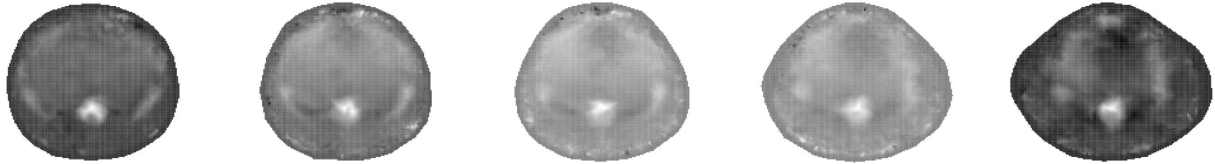


Figure 10. Estimated image using $\alpha = 1.0 \cdot 10^{-16}$, $\beta = 1.0$ and $\gamma = 1.0 \cdot 10^{-6}$

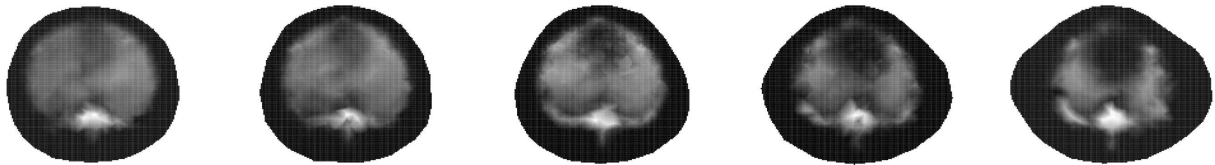


Figure 11. Estimated image using $\alpha = 1.0 \cdot 10^{-16}$, $\beta = 1.0 \cdot 10^{-12}$ and $\gamma = 1.0 \cdot 10^{-6}$

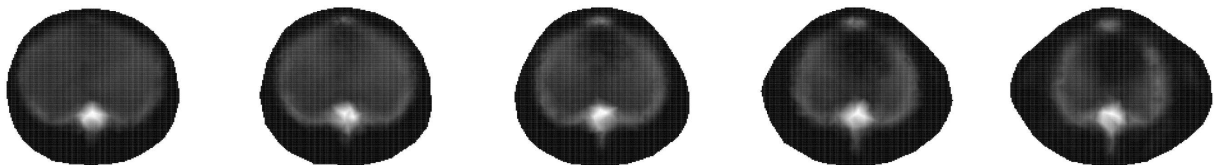


Figure 12. Estimated image using $\alpha = 1.0 \cdot 10^{-16}$, $\beta = 1.0$ and $\gamma = 1.0$

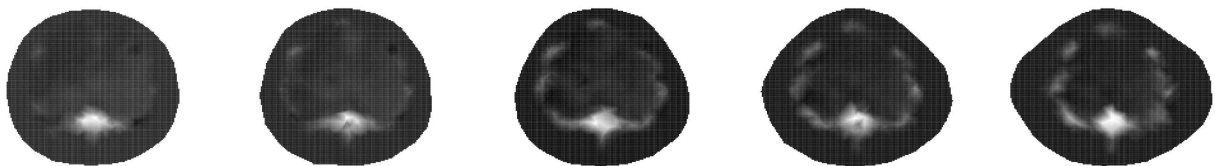


Figure 13. Estimated image using $\alpha = 1.0 \cdot 10^{-16}$, $\beta = 1.0 \cdot 10^{-12}$ and $\gamma = 1.0$

3. Discussion

The results show that it is feasible the assembling of an anatomy and physiology based prior for regularization of the EIT inverse problems based on samples of the population. Qualitatively, the results show that when γ is around 10^{-6} , β is around 10^{-12} and α is around 10^{-16} , the images obtained seem to take into account electric potential measurements and do not follow solely the expected distribution of resistivity and make sense from the anatomical point of view.

The value of α is very low, indicating that the high pass filter is not actually being relevant for the regularization and image estimation. The value of β is also small suggesting that the covariance matrix Γ , which was normalized by the largest variance, has the significant role in the regularization. The results for $\gamma = 1.0$ and for $\gamma = 10^{-6}$ show discontinuous ribs as expected when the image estimation algorithm is taking into account electric potential measurements. Notice that, the expected distribution of resistivity $\bar{\rho}$, has continuous ribs.

4. Final Comments

The objective of the present work was to test the hypothesis that a sample based anatomy based prior for EIT regularization is feasible when the samples take anatomic information from CT-Scans and resistivity information from *in vivo* and *in vitro* measurements. The images obtained clearly follow the electric potential measurements and do not reproduce solely the expected distribution of resistivity, suggesting that the regularization is being effective. The number of CT-Scans available was small, 39, so the covariance matrix and expected distribution of resistivity should not be considered as having high statistical quality. Even with this small number of CT-Scans, the anatomy based prior seems to be able to serve for regularization of the EIT inverse problem.

5. ACKNOWLEDGEMENTS

The researchers acknowledge Faculty of Veterinary Medicine and Polytechnic School of University of São Paulo, Dr. Jari Kaipio for the idea of developing an anatomic based prior for EIT, Gabriela Paola Ribeiro Danon for helping with the CT-scans and the financial support of FAPESP and CAPES.

6. REFERENCES

- Adler, A. and Guardo, R., 1996. "Electrical impedance tomography: regularized imaging and contrast detection". *IEEE Transactions on Medical Imaging*, Vol. 15, No. 2, pp. 170–179.
- Borsic, A., Graham, B.M., Adler, A. and Lionheart, W.R.B., 2010. "In vivo impedance imaging with total variation regularization". *IEEE Transactions on Medical Imaging*, Vol. 29, pp. 44–54.
- de Lima, C.R., Mello, L.A.M., Lima, R.G. and Silva, E.C.N., 2007. "Electrical impedance tomography through constrained sequential linear programming: a topology optimization approach". *Measurement Science and Technology*, Vol. 18, pp. 2847–2858.
- Gabriel, S., Lau, R.W. and Gabriel, C., 1996. "The dielectric properties of biological tissues: Ii. measurements in the frequency range 10 hz to 20 ghz". *Physics In Medicine And Biology*, Vol. 41, pp. 2251–2269. URL <http://niremf.ifac.cnr.it/tissprop/>.
- Haralick, R.M. and Shapiro, M., 1991. *Computer and Robot Vision*. Addison Wesley, Reading.
- Holder, D.S., ed., 2005. *Electrical Impedance Tomography Methods, History And Applications*. Institute of Physics Publishing, London, 1st edition.
- Kaipio, J. and Somersalo, E., 2004. *Statistical and Computational Inverse Problems*. Springer, New York, 1st edition.
- Kaipio, J.K., Kolehmainen, V., Vauhkonen, M. and Somersalo, E., 1998. "Construction of anatomy-based priors with anisotropic characteristics with application to electrical impedance tomography". In *Proceedings of the 20th Annual International Conference of the IEEE Engineering in Medicine and Biology Society*. IEEE, Hong Kong, China, Vol. 20, pp. 1032–1035.
- Kerner, T.E., Paulsen, K.D., Hartov, A., Soho, S.K. and Poplack, S.P., 2002. "Electrical impedance spectroscopy of the breast: clinical imaging". *IEEE Trans. Med. Imaging*, Vol. 21, pp. 638–645.
- Kim, B.S., Isaacson, D., Xia, H., Kao, T., Newell, J.C. and Saulnier, G.J., 2007. "A method for analyzing electrical spectroscopy data from breast cancer patients". *Physiol. Meas.*, Vol. 28, pp. S237–S246.
- Kinouchi, Y., Iritani, T., Morimoto, T. and Ohyama, S., 1997. "Fast in vivo measurements of local tissue impedance using needle electrodes". *Med. Biol. Comput.*, Vol. 35, pp. 486–492.
- Paulson, K.S., Pidcock, M.K. and Mcleod, C.N., 2004. "A probe for organ impedance measurement". *IEEE Transactions on Biomedical Engineering*, Vol. 51, No. 10, pp. 1838–1844.
- Serra, J., 1989. *Image Analysis and Mathematical Morphology*, Vol. 1. Academic Press, London, 3rd edition.
- Steendijk, P.; Murg, G., Veld, E.T.V.D. and Baan, J., 1993. "The four-electrode resistivity technique in anisotropic media: theoretical analysis and application on myocardial tissue in vivo". *IEEE Transactions on Biomedical Engineering*, Vol. 40, pp. 138–148.
- Tsai, J.Z., Cao, H., Tungjitkusolmun, S., J, E.J.W.E., Vorperian, V.R. and Webster, J.G., 2000. "Dependence of apparent resistance of four-electrode probes on insertion depth". *IEEE Transactions on Biomedical Engineering*, Vol. 47, pp. 41–48.
- Vauhkonen, P.J., 2004. *Image Reconstruction in Three-Dimensional Electrical Impedance Tomography*. Ph.D. thesis, Department of Applied Physics, University of Kuopio.

7. Responsibility notice

The authors are the only responsible for the printed material included in this paper.